GO CaBER: Capillary breakup and steady-shear experiments on aqueous Graphene Oxide (GO) suspensions.

Henry C.-H. Ng,[a] Andrew Corker,[b] Esther García-Tuñón,[b] and Robert J. Poole
School of Engineering,
University of Liverpool

(Dated: 9 November 2019)

Synopsis

Aqueous solutions of graphene oxide (GO) with a very large average flake aspect ratio, $AR = O(10^4)$, are probed using capillary breakup experiments and shear rheological measurements for concentrations up to $\phi = 0.4$vol%. Graphene oxide, a chemically oxidized sheet of graphene which we obtained from graphite exfoliation, is suspended in distilled water to produce solutions with volume concentrations spanning $0.02 \leq \phi \leq 0.4$vol%. For concentrations between $0.1 \leq \phi \leq 0.4$vol%, the apparent shear yield stress, τ_y (determined from creep tests), scales with concentration following a power-law relationship with exponent ~ 2.2. Using capillary breakup extensional rheometry (CaBER), we demonstrate that for concentrations $\phi \gtrsim 0.1$vol%, aqueous GO solutions exhibit power-law fluid behaviour in uniaxial elongation. The deformation-rate-dependent transient Trouton ratio over the range where the deformation rates match in shear and capillary breakup experiments is independent of the deformation rate, but inversely proportional to volume concentration with all values exceeding three. An attempt is made to estimate the apparent elongational yield stress (for $\phi \geq 0.3$vol%) by using the Laplace pressure within the fluid filament as its surrogate and we find that in the strain rate regime that we can observe, the apparent elongational yield stress, $\tau_{y,e}$ is not $\sqrt{3}$ times the shear yield stress, i.e. for our aqueous GO solutions we are not able to observe agreement with the von Mises plasticity criterion. GO samples at a given concentration probed in capillary breakup extensional rheology experiments under different protocols, i.e. slow-retraction opposed to step-stretch, exhibited different responses confirming that GO is highly sensitive to the deformation history, however, they still exhibit power-law fluid behaviour even given the different initial conditions. Although slightly limited in our ability to quantify the extension-thinning yield-stress-like behaviour of aqueous GO in uniaxial elongational flow by the fact that we cannot prescribe the strain rates in CaBER experiments, we demonstrated that even a very small amount of GO flakes can significantly alter the shear rheology and the pinch-off dynamics of a liquid bridge in comparison to Newtonian fluids of equivalent shear viscosity.

Keywords: Graphene Oxide, Capillary thinning, Yield stress, Elongational flow, Shear rheology, Extensional rheology.

I. INTRODUCTION

Graphene Oxide (GO) is a chemically oxidized sheet of graphene. Single sheets of graphene, a 2D monolayer of carbon atoms, were successfully isolated in laboratory experiments less than two decades ago (Novoselov et al., 2004; Geim and Novoselov, 2007; Eda et al., 2008). Since that time, numerous applications in biomedical, electrical and materials engineering have been identified as ideal for its use due to the extraordinary physical properties that graphene possesses. Pristine graphene is difficult to produce in large quantities and a chemically modified version; graphene oxide is more commonly encountered.

[a] hchng@liverpool.ac.uk
[b] Also at: Materials Innovation Factory, University of Liverpool

Graphene Oxide is a 2D monolayer of carbon atoms containing several oxygen functional groups and it is the distribution of the functional groups on the basal plane (hydroxl, epoxy and unoxidized graphitic islands) and edges (carboxylic and hydroxl groups) that gives GO its unique properties García-Tuñón et al. (2017). The shear rheology of aqueous GO has been reported in previous studies over a wide range of concentrations, see, for example: Tiwari et al. (2013); Vasu et al. (2013); Naficy et al. (2014); Vallès et al. (2014); Del Giudice and Shen (2017); García-Tuñón et al. (2017); Del Giudice et al. (2018). Those works have reported that in shear flow, aqueous solutions of GO exhibit many interesting properties; at higher concentrations it has been demonstrated that GO flakes in aqueous suspensions form ordered clusters analogous to liquid crystalline structures; (see, for example: Xu and Gao (2011); Jalili et al. (2013); Kumar et al. (2014)). Naficy et al. (2014) describe GO dispersions as a "new class of soft materials" possessing rich and unique properties somewhere between 2D nanoplatelets and 1D polymers Cheng and Li (2013), with GO flakes shown to be soft sheets that can fold and wrinkle Allen et al. (2010) whilst being simultaneously highly flexible Poulin et al. (2016) and surface active in nature Chen et al. (2009); Kim et al. (2010a,b), due to the combination of hydrophilic functional groups (-COOH, -OH and -O-) decorating the flake basal plane and the edges, combined with regions of the basal plane that remain unoxidized (hydrophobic islands). Aqueous GO solutions are known to be shear thinning; when dispersed in low concentrations the GO flakes tend to aggregate, and the existence of thixotropy, shear banding and a finite apparent shear yield stress has been reported for volume concentrations as low as $\phi \approx 0.04$vol% by Vasu et al. (2013) and $\phi \approx 0.02$vol% by Naficy et al. (2014), albeit at average GO flake aspect ratios of $AR = O(10^3)$ and $AR = O(10^4)$, respectively. Whilst many works have addressed the phenomenon of an apparent yield stress in soft matter Hartnett and Hu (1989); Nguyen and Boger (1992); Bonn and Denn (2009); Balmforth et al. (2014), they mostly do so in the context of simple shear flows. Recently, more work has been done on understanding the apparent elongational yield stress Niedzwiedz et al. (2009, 2010); Balmforth et al. (2010); Martinie et al. (2013); Louvet et al. (2014); Valette et al. (2019) and we will essentially follow the methodology outlined in Martinie et al. (2013) when attempting to estimate the apparent elongational yield stress from our capillary breakup experiments on aqueous GO solutions. The foundation of the methodology in Martinie et al. (2013) is not dependent on a constitutive equation or model and is based on an observation that 'yield-stress' fluids can form stable cylinders with length larger than their circumference and that the filament deformation and onset of thinning is determined by the apparent elongational yield stress Lowry and Steen (1995); Mahajan et al. (1999).

Characterization of *both* the shear and extensional rheology in complex fluids is important as the elongational flow behaviour may not be well described by simple generalised Newtonian fluid (GNF) constitutive equations and whilst the shear response of aqueous GO solutions has been widely reported, very little has been reported regarding the extensional flow behaviour of these fluids. Thus the primary aim of the current work is to shed light on the extensional properties of aqueous graphene oxide solutions formed using ultra-large GO sheets ($AR = O(10^4)$) at volume concentrations close to the onset of a finite apparent shear yield stress ($0.02 \lesssim \phi \lesssim 0.4$vol%) reported in the literature Vasu et al. (2013); Naficy et al. (2014). We will do this by probing the response of our GO solutions in uniaxial extension using a capillary breakup extensional rheometer (CaBER) and complement this with shear flow measurements; attempting to relate material properties of aqueous GO in shear and extension. The rest of the paper will be structured as follows: the methods and materials will be described in section II followed by the results and discussion of the shear experiments in section III and the capillary breakup experiments in section IV with conclusions presented in section V.

II. EXPERIMENTAL SETUP

A. Materials

The sample preparation and characterization of the GO solutions used in this study was previously reported in Corker et al. (2019) and will only be briefly summarized here.
GO was produced by graphite exfoliation using the modified Hummers method García-Tuñón et al. (2015); Rocha et al. (2017) inside a jacketed reactor with 24g of graphite chemically exfoliated using strong oxidizing agents. This produced around 3L of graphene oxide "stock" slurry, that once washed, was at approximate volume concentration of $\phi = 0.4$vol%. The procedure was as follows; 24g of high quality graphite flakes were first placed into the reactor, followed by the addition of 5300g of sulphuric acid (H_2SO_4) (97wt%) and 544g of phosphoric acid which were fed into the reactor using a peristaltic pump. With the temperature kept constant at $T = 50°$C, 144g of $KMnO_4$ was slowly added over the next 18 hours. The temperature was then lowered to $T = 20°$C prior to adding 1600g of water along with 120g of H_2O_2 (30wt%). Once cooled down, the reactor contents were drained into plastic bottles for centrifugation to complete the exfoliation of GO flakes. The first centrifugation cycle lasted an hour with the speed set to 9000rpm. This was followed by additional centrifugation cycles until the supernatant became clear. The supernatant was then drained and replaced with approximately 2L of distilled water. Finally, the washing process was repeated fourteen times at five hour centrifugation cycles. When the pH of supernatants was ~ 5, and most of the remaining acids in solution were washed. The "stock" GO solution ($\phi = 0.4$vol%) was then further diluted using distilled water to produce the GO solutions at the lower concentration, with solution density close to that of water i.e. $\rho \approx 1000\text{kg/m}^3$.
The GO stock solution had a pH = 2.2 (measured using a *Mettler Toledo SevenCompact* S210 pH-meter) and volume concentration of $\phi = 0.4$vol%. The lateral flake size, determined from optical microscopy (*Olympus BX-53*), ranged from ~ 11 to $\sim 230\mu$m with a mean size of $\sim 64\mu$m (which we note is larger than most of the flake sizes reported in the literature by, for example, Xu and Gao (2011); Vasu et al. (2013); Vallès et al. (2014); Kumar et al. (2014); Del Giudice et al. (2018)). Our lateral flake size yields an average flake aspect ratio of $AR = O(10^4)$ assuming that the flake thickness is $1 \sim 2$nm, which is the flake thickness that has been typically reported in the literature Naficy et al. (2014); Vasu et al. (2013); Del Giudice et al. (2018); Tiwari et al. (2013). The surface tension was measured for GO solutions with volume concentrations $0.1 \leq \phi \leq 0.4$vol% using the pendant drop method on a *Kruss* DSA100 Drop Shape Analyzer. The obtained surface tension values were $\sigma = 68 \pm 1$, 56 ± 2, 29 ± 2 and $26 \pm 2\text{mNm}^{-1}$ for volume concentrations $\phi = 0.1$, 0.2, 0.3 and 0.4vol%, respectively. The drop in surface tension between concentrations $\phi = 0.2$vol% and $\phi = 0.3$vol% is likely due to the surface active nature of the GO sheets which have been shown to be amphiphilic owing to the presence of hydrophilic oxygen functional groups (-COOH, -OH and -O-) attached to the otherwise hydrophobic sheet basal plane and edges Chen et al. (2009); Kim et al. (2010a,b). For volume concentrations below $\phi = 0.1$vol%, we have assumed that the surface tension is that of the solvent $\sigma = 72\text{mNm}^{-1}$ and surface tension values for $\phi \geq 0.1$vol% which were not directly measured were obtained by linear interpolation from the measured values. Elemental chemical analysis (*Thermo Scientific Flash 2000*, configured for %CHNS) was carried out on the freeze-dried GO powders to determine the composition and degree of oxygenation of the current batch. On average, the GO powders consisted of 37.6wt% (C)arbon, 2.2wt% (H)ydrogen and 0wt% (N)itrogen with the remaining (O)xygen content estimated to be 60.2wt%, yielding a C/O ratio of 0.66, which is higher oxygenation than previous batches García-Tuñón et al. (2015, 2017).

B. Shear rheometry

Shear-flow measurements were conducted on an *Anton Paar* MCR302 rheometer using a roughened, stainless-steel parallel-plate geometry of diameter $D_{plate} = 50$mm at a gap size 1mm. A roughened geometry was selected to minimize the wall slip effect reported in Vasu et al. (2013). A solvent trap was employed to prevent evaporation during measurements which were conducted at a constant temperature of $T = 20°$C. The samples were pre-sheared for 180 seconds at a shear rate of $\dot{\gamma} = 10^3 \text{s}^{-1}$ and then rested for 60 seconds to provide a constant deformation history. Following the pre-shearing step, measurements were conducted at a range of constant stress values each for a period between 1200s and 1800s, with the range of the applied stress dependent on the concentration. These creep tests (Nguyen and Boger, 1992) were carried out at applied stresses above and below the estimated yield value with the creep compliance $J(t) = \gamma/\tau_{yz}$ monitored over time, where γ is the strain and τ_{yz} the applied stress. Once the applied stress exceeded the yield stress for a given concentration; the time series of each of the transient measurements was carefully inspected to determine if an equilibrium value of shear rate could be reached within the measurement time i.e. to check whether the transient apparent viscosity η^+ would become time invariant. Only for those applied stresses where a steady state could be reached were the data averaged over the appropriate times to derive an equilibrium value of steady shear viscosity η. The effect of preshear on the obtained steady-state viscosity was tested by varying the applied preshear between $\dot{\gamma} = 100\text{s}^{-1}$ and 1000s^{-1} and between durations of 10s and 180s for two representative concentrations ($\phi = 0.1$vol% and 0.2vol%) and applied stresses ($\tau_{yz} = 12$Pa and 30Pa), respectively. We found that our choice of pre-shear had only a minimal effect on the steady-state viscosity with no more than a $\pm 8\%$ peak-to-peak variation and no systematic effect of total shear strain applied was observed.

C. Extensional rheometry

Capillary Breakup Extensional Rheometery (CaBER) is commonly used to probe the extensional properties of fluids McKinley and Tripathi (2000); Anna and McKinley (2001). In these experiments, an unstable fluid filament is set up between two parallel plates where a subsequent uniaxial extensional flow develops as the fluid filament undergoes capillary thinning. By tracking the time evolution of the filament diameter, several properties can be extracted from CaBER measurements which include the critical time to breakup t_c and the apparent extensional viscosity $\eta_{app,ext}(\dot{\varepsilon})$. The strain rate $\dot{\varepsilon}$ of a cylindrical fluid filament is given by;

$$\dot{\varepsilon} = -\frac{2}{R_{mid}(t)}\frac{dR_{mid}(t)}{dt} \tag{1}$$

where R_{mid} is the filament radius at mid-height. If inertia can be neglected, the fluid filament selects a self-similar force balance between capillary pressure and visco-(elasto) stresses (Papageorgiou, 1995; Anna and McKinley, 2001) and the apparent extensional viscosity can be determined from;

$$\eta_{app,ext} = \frac{\Delta\tau}{\dot{\varepsilon}} = \frac{\sigma/R_{mid}(t)}{\dot{\varepsilon}} = \frac{\sigma}{2dR_{mid}(t)/dt}, \tag{2}$$

where σ represents surface tension. In practice the apparent extensional viscosity, $\eta_{app,ext}$, is given by;

$$\eta_{app,ext} = \frac{(2X-1)\sigma}{2dR_{mid}(t)/dt} \tag{3}$$

where it has been shown in experiments (McKinley and Tripathi, 2000) and simulations (Papageorgiou, 1995) that $X = 0.7127$ for viscous Newtonian filaments. The correction

factor is required because the force balance leading to equation (2) assumes an axially uniform thread (Entov and Hinch, 1997) but in reality, while the thread may become slender, it is never truly uniform McKinley and Tripathi (2000).

In addition to the apparent extensional viscosity, the apparent elongational yield stress $\tau_{y,e}$ can also be estimated from CaBER measurements. According to Martinie et al. (2013), setting the Laplace pressure inside the filament to the apparent elongational yield stress is justified assuming the filament has a cylindrical shape and that $\tau_{xx} = 0$, i.e. the normal stress in the filament axial direction. The *initial plateau of the Laplace pressure* at the location of the filament minimum diameter can be considered as the apparent elongational yield stress of the material. The Laplace Pressure ΔP within a liquid thread is related to the radius R and axial curvature κ of the filament;

$$\Delta P(x,t) = \sigma \left(\frac{1}{R(x,t)} - \kappa(x,t) \right), \tag{4}$$

with;

$$\kappa(x,t) = \left| \frac{\left(\partial^2 R(x,t)/\partial x^2\right)}{\left[1 + \left(\partial R(x,t)/\partial x\right)\right]^{3/2}} \right|. \tag{5}$$

At low volume concentrations, the GO solutions have a low viscosity and filaments break before the piston is stopped when applying a step-strain. Therefore, we only attempt to estimate the elongational yield stress on GO solutions with $\phi = 0.3$ and 0.4vol%. These samples were loaded into the CaBER with an initial plate gap of h_0 and stretched to a final gap of h_f within a stretching time of t_s. We have used a plate diameter of $2R_0 = 4$mm and an initial gap $h_0 = 2$mm for samples with $\phi = 0.3$vol% and $h_0 = 3$mm for samples with $\phi = 0.4$vol%. The samples are then stretched to their final height(s); $3.78 \leq h_f/h_0 \leq 6.57$ for $\phi = 0.3$vol% and $2.99 \leq h_f/h_0 \leq 4.76$ for $\phi = 0.4$vol%, respectively, all over a time of $t_s = 35$ms (with a minimum of 3 repeats). This resulted in corresponding Hencky strain rates in the range $37 \lesssim \dot{\epsilon_H} = \ln\left(h_f/h_0\right) \times 1/t_s \lesssim 54\text{s}^{-1}$ and $31 \lesssim \dot{\epsilon_H} \lesssim 45\text{s}^{-1}$.

For all other CaBER measurements on GO solutions with concentrations between $0.02 \leq \phi \leq 0.4$vol% we adopt the so-called "slow retraction method" (SRM) a modified operational protocol for the CaBER device developed to minimize the effect of inertia on low viscosity fluids Campo-Deaño and Clasen (2010). Instead of applying a step strain to the sample; the liquid bridge is instead brought close its stability limit before the end plates are driven apart at a very slow velocity (~ 0.2mm/s) to initiate the filament breakup process. Campo-Deaño and Clasen (2010) introduced the SRM to probe the extensional viscosity of elastic fluids with ultra-short relaxation times and we use essentially the same protocol reported in that study for our experiments even though our fluids are essentially inelastic.

All our capillary-thinning experiments were carried out using a commercial *THERMO Haake CaBER-1* extensional rheometer which consists of two parallel circular end plates of diameter $2R_0 = 4$mm set to an initial gap of $L_0 = 2$mm. The initial gap is set by manually traversing the bottom plate with a micrometer (*Holex T0503-100A* $0 - 25$mm, Resolution 0.002mm) and then positioning the top plate with the device's motor drive. During the experiments the bottom plate remains stationary and the top plate is pulled upwards at a constant velocity.

Filaments were backlit using a *ThorLabs OSL2 FiberIlluminator* and viewed through a microscope objective connected to an *IDT XS5-M-4* high-speed camera (Integrated Design Tools, Inc. USA, 1280×1024) via an extension tube which yielded a spatial resolution of 1.97μm/pixel at maximum magnification of $6\times$. Images were acquired at up to 6040 frames per second (fps) by reducing the region of interest (ROI) to 1280×176 pixels. This limited the field-of-view (FOV) to 2.52×0.35mm (height-by-width) at maximum magnification. As a result, images of the filament evolution are limited to the latter stages of thinning i.e. only when the filaments are narrow enough to enter the FOV. The image acquisition rate was adjusted according to the filament lifetime; for example, CaBER measurements using the SRM of GO solutions at low concentration (and hence low viscosity) were conducted at

the maximum rate as filament lifetimes were in the order of milliseconds, but measurements used to estimate the apparent elongational yield stress were conducted at much slower acquisition rates as the filament lifetimes were in the order of seconds.
Images of the filament evolution and breakup were processed in MATLAB® using bespoke routines written in house. The images are first thresholded to maximize the contrast at the interface between the liquid filament and surrounding air. The liquid/air interface is traced with the "Canny" edge detection routine in-built in MATLAB® (Canny, 1986). The filament minimum diameter is tracked in time without resorting to curve fitting along the filament axial direction and the filament curvature κ in equation (5) is calculated by differentiating the filament profiles using in-built MATLAB routines after smoothing the filament profiles in the axial direction using a median filter with a fitting window of 7 points. Due to the limited FOV at maximum magnification; the filament diameter $2R(x)$, where x is the longitudinal direction along the filament axis, is only tracked towards the latter stages of evolution and ultimate breakup.

III. SHEAR RHEOLOGY

Creep tests were carried out for a different range of applied stresses for each concentration in the range $0.02 \leq \phi \leq 0.4$vol% to determine the yielding behaviour of the aqueous graphene oxide suspensions. We monitor the creep compliance $J(t) = \gamma/\tau_{yz}$ as a function of time; below the apparent yield stress, the creep compliance $J(t) = \gamma/\tau_{yz}$ will become constant at long times. When the applied stress exceeds the apparent yield value, the creep compliance will grow continually with time and we define the apparent yield stress τ_y as the lowest imposed stress for which the compliance no longer tends to a constant value (Dinkgreve et al., 2016). Creep compliance J for a representative volume concentration of $\phi = 0.3$vol% is shown in figure 1(a). It is easy to distinguish between un-yielded and yielded behavior for GO solutions with $\phi = 0.3$vol%; for applied stress $\tau_{yz} \leq 4.0$Pa, the creep compliance tends to an equilibrium value at long times. When the applied stress is increased to $\tau_{yz} = 5.0$Pa; the creep compliance increases monotonically with time, far exceeding the value of $J(t)$ at long times when the applied stress level was $\tau_{yz} = 4.0$Pa, indicating a yielded behavior. The yielding characteristics are also reflected in the transient viscosity η^+ (figure 1b); when unyielded, the transient viscosity increases with time (as the shear rate decreases) and eventually very large fluctuations appear in the transient viscosity which Vasu et al. (2013) describes a "jammed" state. Once yielded, (applied stress $\tau_{yz} > 5$Pa), the transient viscosity decreases gradually with time (where an inflection is seen in the transient viscosity curves) and finally, at applied stress $\tau_{yz} >> \tau_y$ i.e. $\tau_{yz} \geq 20$Pa, the transient viscosity decreases rapidly with time before reaching a steady-state value beyond $t \approx 200$s (figure 1c). Vasu et al. (2013) describes this state, where there exists a steady-state value of viscosity as "shear-induced rejuvenation". Within the intermediate state between that of "jamming" and "rejuvenation" no steady-state exists (at least over the time scales we have investigated). Below a volume concentration of $\phi = 0.1$vol%; the creep compliance did not tend to constant value within our measurement time (even for applied stresses near the limit of rheometer resolution) hence we could not determine a yield stress for $\phi < 0.1$vol%. The apparent yield stresses that were measurable from our creep tests are plotted as a function of volume concentration in figure 2 and shown to scale approximately as $\tau_y \sim \phi^{2.2}$. Although our tests were conducted over a small range of concentrations, the power-law exponent agrees well with what has been reported by Vasu et al. (2013) ($AR = O(10^3)$) and Naficy et al. (2014)($AR = O(10^4)$) who both report a scaling exponent of $\sim 2.5 \pm 0.1$ and Del Giudice et al. (2018) $\sim 2.35 \pm 0.86$ ($AR = O(10^2)$), hence there does not appear to be a clear relationship between the scaling exponent for the apparent shear yield stress and the average GO flake aspect ratios where in the current study we have used GO sheets with $AR = O(10^4)$.

The steady-state shear viscosity is shown as a function of deformation (shear) rate in

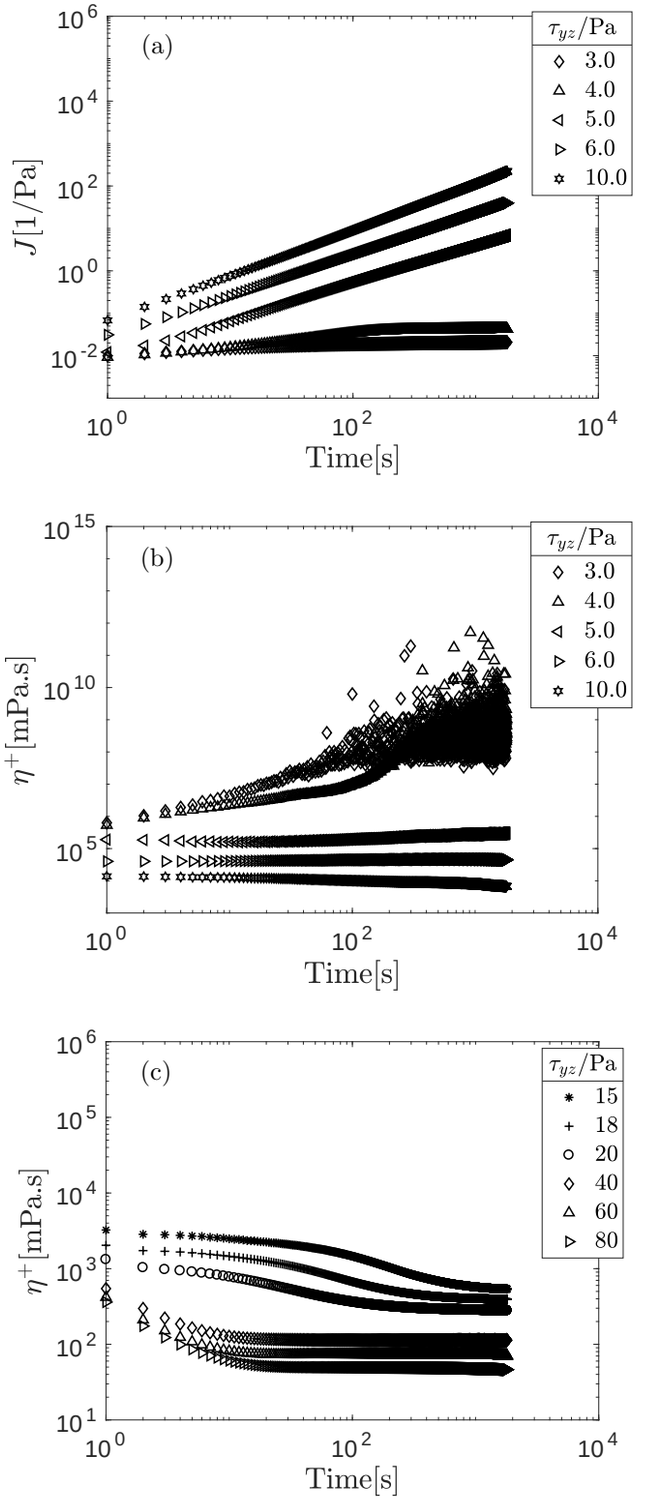

FIG. 1: (a) Creep compliance J and (b) corresponding apparent transient viscosity. (c) Apparent transient viscosity for applied stress far beyond initial yielding for a representative volume concentration of $\phi = 0.3$vol%.

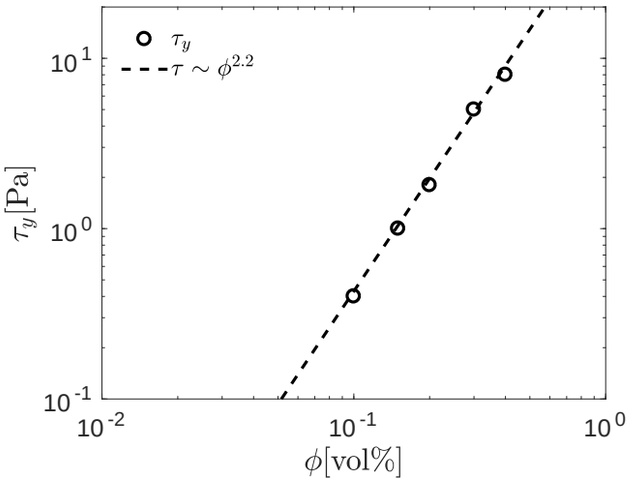

FIG. 2: Apparent shear yield stress determined from creep tests.

figure 3 to facilitate a comparison to apparent extensional viscosities obtained from CaBER measurements. These shear viscosities are obtained from transient measurements by averaging only over the steady-state values of the time histories (per applied stress value) which are typically over the last 200 to 800s of the measurement. As steady-state viscosity values could only be reached in the so-called "shear rejuvenated" state which only occurs at intermediate-to-high applied stresses; the shear rate is relatively large $\dot{\gamma} = O(10^1)$ to $O(10^3)\text{s}^{-1}$, however, this is within the range of deformation rates observed in the capillary breakup experiments. From figure 3 we see that GO solutions with volume concentration $0.02 \leq \phi \leq 0.4$vol% are shear thinning indicating that our GO solutions exhibit power-law fluid behaviour over this range of shear rates. For a power-law fluid, the variation of shear stress $\tau_{yz} = K\dot{\gamma}^m$ with shear rate is described by a power law index, m, and consistency factor, K. Power-law fits to the shear stress versus shear rate data (not shown here) yielded scaling exponents between $m = 0.81$ and $m = 0.44$ for concentrations between $0.02 \leq \phi \leq 0.4$vol% (for the shear rate range shown in figure 3). To check the sensitivity of the measured apparent yield stress and the steady state shear viscosity to gap height, measurements were repeated for a gap size of $h = 1.2$mm at a representative volume concentration of $\phi = 0.3$vol% and we find that while the precise values of creep compliance for a given time differ with measurement gap, the applied stress to cause yielded behviour does not. A second set of measurements conducted for a representative concentration of $\phi = 0.2$vol%; applied stress of $\tau_{yz} = 30$Pa for measurement gaps of $h = 1.0$, 1.2, 1.6 and 2.0mm yielded a nominally constant apparent shear rate (to within our measurement reproducibility of $\pm 8\%$). While not necessarily a definitive assessment due to the limited range of measurement gaps investigated, a constant apparent shear rate for different measurement gaps implies that our measured data are free of potential wall-slip effects. Measurements where the applied stress corresponded to the "shear rejuvenation" regime Vasu et al. (2013) were not sensitive to a variation in the measurement gap.

IV. EXTENSIONAL RHEOLOGY

A. The apparent extensional viscosity and transient Trouton ratio

At concentrations below $\phi < 0.10$vol% the capillary thinning and breakup process that we are able to observe, given the limited FOV, occurs approximately over a duration of

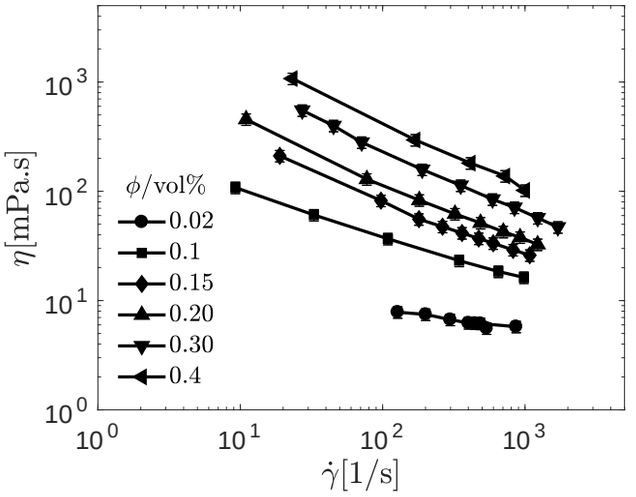

FIG. 3: Viscosity derived from transient measurements by averaging only over the period after a steady-state shear rate was achieved (typically the last $200 \sim 800$s) for each applied stress. Error bars indicate $\pm 8\%$ of final value indicating estimated measurement repeatability based on application of different pre-shears applied prior to constant stress measurements.

$\Delta t = 2$ms. For example, for GO $= 0.02$vol%, the liquid-air interface of the filament does not enter the FOV until approximately three images prior to breakup or approximately $t = -0.83$ms (inset images in figure 4a). The axial location of breakup is also not at the filament mid-height, but rather, at the two end-drops. This occurs because the thinning rate or capillary velocity is so high that inertia dominates (due to low viscosity) and the flow becomes almost purely inertia controlled. This regime is the so-called potential flow (PF) regime Campo-Deaño and Clasen (2010) and can be described by a power law (independent of fluid viscosity);

$$\frac{R\,(t)}{R_0} = 0.64 \left(\frac{\sigma}{\rho R_0^3}\right)^{1/3} (t_c - t)^{2/3} \tag{6}$$

derived by Day et al. (1998); Rodd et al. (2005). Here, $R(t)$ is the filament radius as a function of time, $R_0 = 2$mm the initial radius (which we take as the radius of the end plates employed in the CaBER) , σ the surface tension, ρ fluid density and t_c the filament breakup time. The scaled radius evolution $R(t)/R_0$ is plotted against time (normalised with breakup time) $t_c - t$ in figure 4 for selected concentrations on logarithmic axes. For $\phi = 0.02$vol%, we see that the radius evolution along the filament midheight (circle symbols in figure 4a) scales according to a power law $n = 2/3$ predicted for inertia dominated capillary breakup (equation (6)). From the inset photos, we can see that the filament is curved and does not form a cylinder prior to break up. Hence, we extract the filament radius evolution at different axial locations to check the decay rate. We find that for $\phi = 0.02$vol%, the radius evolution for axial locations $x = \pm 0.1$mm from the midheight still scales according to a power law with exponent $n = 2/3$ (triangle symbols in figure 4a) and that the radii values at the different axial locations agree well indicating that the filament is approximately symmetric. The variation in the radius values at $t_c - t \approx 3 \times 10^{-4}$s are due to the filament bulging prior to breakup at the two end-drops, a qualitative signature of inertia controlled breakup. When increasing the volume concentration to $\phi = 0.05$vol% (figure 4b) we observe a visco-capillary response as the radius evolution now scales linearly with time and we see that the thinning rate also appears fairly insensitive to the axial location as we see that the radius evolution extracted at $x = \pm 0.2$mm from the midheight also scale linearly with time. Again, the good agreement between radii values above and below the filament midheight

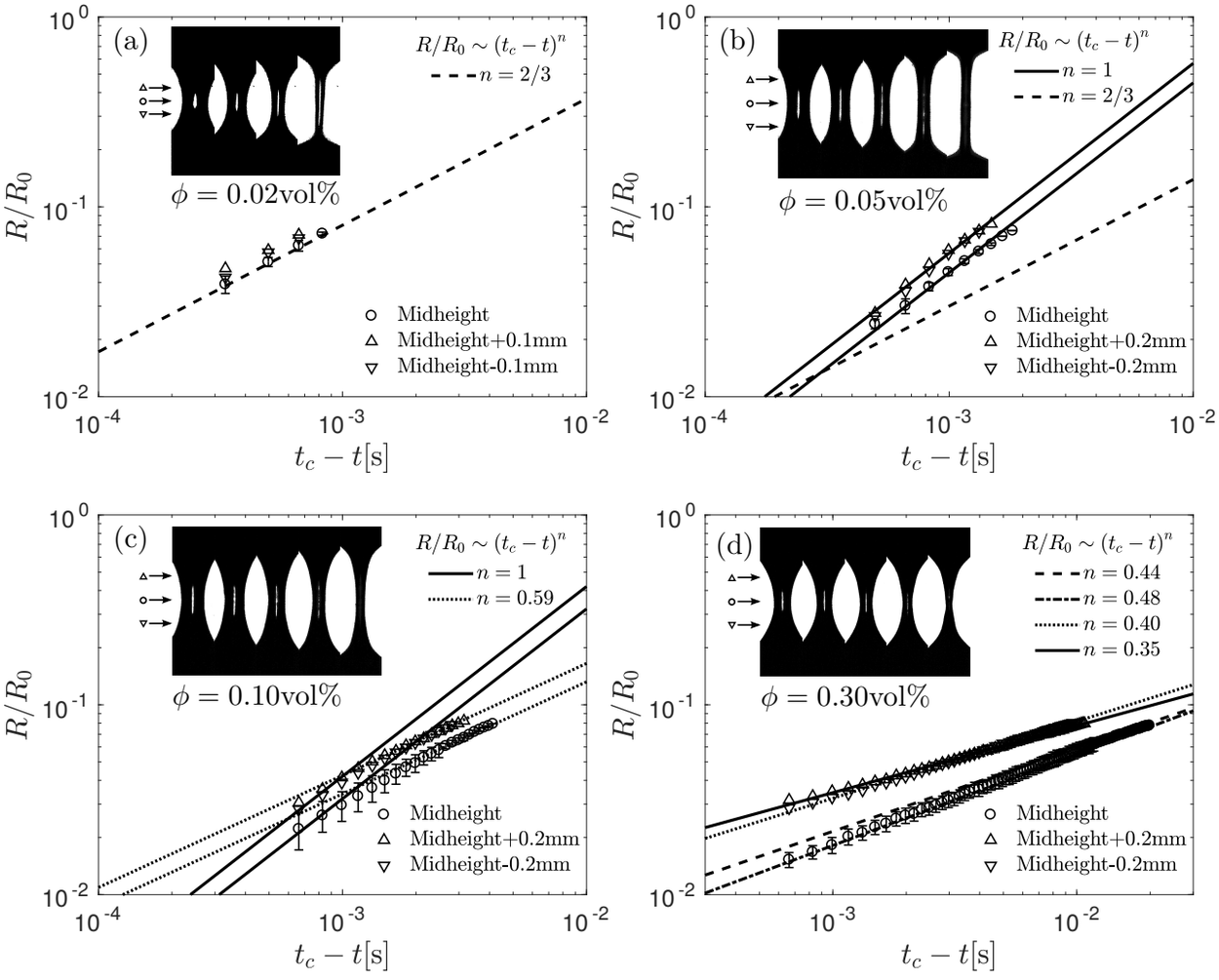

FIG. 4: Normalised filament radius evolution over time as the pinch-off instant is approached from right to left for selected concentrations of graphene oxide suspensions. (a) $\phi = 0.02$vol%; dashed line represents power law with exponent $n = 2/3$ representative of inertia dominated (potential) flow Day et al. (1998). Time step between images ≈ 0.17ms. (b) $\phi = 0.05$vol%, solid lines represents power law with exponent $n = 1$ indicative of visco-capillary Papageorgiou (1995) (or inertio-visco-capillary Eggers (1993)) flow with dashed line indicative of potential flow show together for comparison. Time step between images ≈ 0.17ms. (c) $\phi = 0.10$vol%, solid line is power law with exponent $n = 1$ and dashed line represents power law with exponent $m = 0.59$ (obtained from shear flow measurements). Time step between images ≈ 0.34ms. (d) $\phi = 0.30$vol%; dashed line represents power law with exponents $m = 0.44$ (obtained from shear measurements); dot-dashed line $n = 0.48$ obtained from fit to plotted radius data at filament midheight and dotted and solid lines represent power laws with exponent $n = 0.40$ and $n = 0.35$ obtained by fitting to the CaBER data at locations above and below the filament midheight, respectively. Time step between images ≈ 0.83ms. All figures: arrow shows axial location of measured radius corresponding to symbols plotted. Error bars plotted for filament evolution at midheight represents variation over repeated measurements.

indicate that the filaments are close to symmetric. In the absence of inertia; Papageorgiou (1995) predicted that the filament radius decreases linearly with time according to;

$$\frac{R_{mid}(t)}{R_0} = 0.0709\frac{\sigma}{\eta R_0}(t_c - t). \tag{7}$$

The evolution equation (7) assumes that inertia is negligible, Eggers (1993), however, shows that at the very late stages of thinning, the capillary velocity becomes so high that inertia becomes important again and that the filament diameter evolves according to;

$$\frac{R_{mid}(t)}{R_0} = 0.0304\frac{\sigma}{\eta R_0}(t_c - t). \tag{8}$$

While it is true that the filament thinning rate will yield the capillary velocity (σ/η) according to either equation (7) or (8), we cannot determine whether we are in the visco-capillary regime Papageorgiou (1995) or the inertio-visco-capillary regime Eggers (1993) without direct observation of the scaling transition. Therefore, for our CaBER measurements which exhibit a Newtonian response (where $0.02 \leq \phi \leq 0.075$vol%), we have not attempted to back calculate the shear viscosity η. Capillary breakup experiments on solutions with $\phi = 0.04$vol% and $\phi = 0.075$vol% also exhibited Newtonian dynamics and are not shown here for brevity.

In brief, we are able to say that for $\phi \leq 0.02$vol%, the capillary thinning and breakup process is essentially identical to that of water in our CaBER tests i.e. both are nearly purely inertia driven and that between a concentration $0.04 \lesssim \phi \lesssim 0.075$vol%, the time evolution of the filament diameter appears linear and therefore similar to a Newtonian fluid. Our observations up to this point can be explained by the fact that during CaBER experiments, the experimentalist is not able to directly prescribe the deformation rate and that it is the properties of the working fluid that determine the rates encountered during the experiment. At concentrations up to $\phi \leq 0.075$vol%, we have simply fallen outside the operating range for CaBER measurements even using the SRM. Estimates of the viscosity corresponding to the lower working limit for CaBER experiments using standard step stretch protocols are $\eta \approx 70$mPa.s Rodd et al. (2005) which are reduced to $\eta \approx 27$mPa.s when using the SRM Campo-Deaño and Clasen (2010). A recently developed technique "dripping-onto-substrate" (DoS) Dinic et al. (2017); Sur and Rothstein (2018) enables extensional rheological measurements to viscosities as low as $\eta = 1$mPa.s. This DoS technique may allow us to overcome the limitations of the SRM and is the subject of future work but is beyond the scope of the current manuscript.

At a concentration of GO = 0.1vol% (figure 4c) we see a clear change in quantitative behaviour with the emergence of power-law scaling for the radius evolution; a scaling exponent of $m = 0.59$ which is obtained from shear rheometry provides a good fit to the radius evolution for the early stages of thinning, however, towards the late stages as the deformation rates become increasingly large, the local scaling exponent increases towards $n = 1$ indicative of Newtonian dynamics. This transition from a shear-thinning power-law response to a Newtonian-like response is also shown for radii evolution profiles extracted at axial locations $x = \pm 0.2$mm above and below the filament midheight. Interestingly, there is little to suggest from the inset images of the filament profiles that the filament radius at this concentration would exhibit power-law scaling as we do not observe a conical tapering along the filament axis that is the visual signature of shear-thinning power-law fluids in capillary breakup experiments. The radii evolution for power-law fluids can be represented as McKinley (2005); Balmforth et al. (2010); Niedzwiedz et al. (2010);

$$\frac{R(t)}{R_0} = \Phi(n)\frac{\sigma}{K}(t_c - t)^n \tag{9}$$

where n is the power-law exponent, K is the consistency factor and $\Phi(n)$ is a numerical constant. The aforementioned conical tapering prior to breakup however, is very apparent for a volume concentration of $\phi = 0.3$vol% (figure 4d); rather then approaching a straight

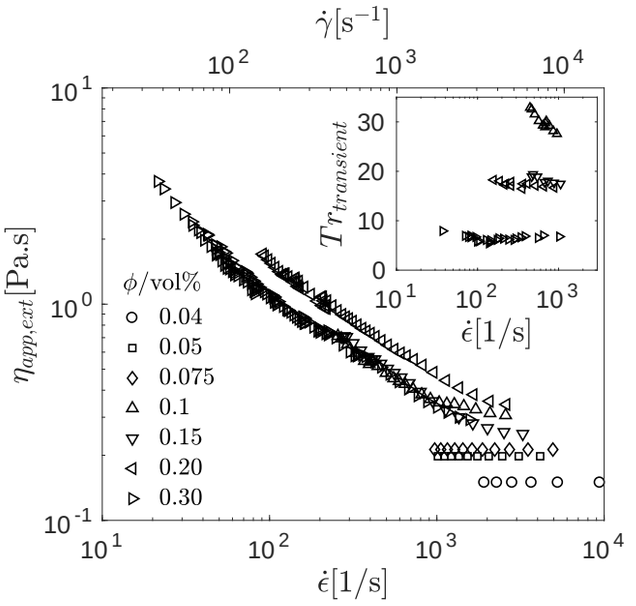

FIG. 5: Apparent extensional viscosity, $\eta_{app,ext}$, as a function of strain rate, $\dot{\epsilon}$, calculated at filament midheight. Inset plot shows the transient apparent Trouton ratio $Tr_{transient}$ calculated by setting shear rate $\dot{\gamma} = \sqrt{3}\dot{\epsilon}$ and obtaining η_s from steady shear measurements presented in section III.

cylinder, the filament forms a conical taper near breakup; and there is a pronounced "necking" prior to final breakup. The time evolution of the filament radius shows an extended region of constant slope and the scaling exponent of $n = 0.48$ obtained by fitting equation (9) to the plotted data is shown to provide fairly good agreement with the power-law exponent of $m = 0.44$ obtained from shear flow, although $m = 0.44$ clearly provides a better fit at early times in the filament evolution. Away from the filament midheight, a scaling exponent of $n = 0.48$ does not provide a good agreement to the measured CaBER data and we can see that the decay rate is different for the radius evolution extracted at $x = \pm 0.2$mm above and below the filament midheight with scaling exponents of $n = 0.35$ and $n = 0.4$ obtained from fitting the filament radii data extracted at those locations, respectively. Notably, both scaling exponents (away from the midheight) are less than $n = 0.48$. For volume concentrations $\phi = 0.15$vol% and 0.2vol% (not shown for brevity), power-law exponents obtained by fitting equation (9) to the filament evolution at midheight yielded $n = 0.52$ and 0.53 compared to $m = 0.48$ and $m = 0.45$ obtained from shear flow measurement, respectively.

The apparent extensional viscosity $\eta_{app,ext}$ is calculated using equation (3) from the radii evolution extracted at filament midheight and plotted against strain rate (equation (1)) in figure 5. For concentrations that exhibited Newtonian dynamics ($0.04 \leq \phi \leq 0.075$vol%), the radius evolution profiles were fitted with a first order polynomial prior to differentiating, hence we obtain constant extensional viscosities (as expected for Newtonian dynamics). At these concentrations; $\eta_{app,ext}$ increases monotonically with concentration and $100 \lesssim \eta_{app,ext} \lesssim 250$mPa.s. Assuming that at infinite shear rates, aqueous GO solutions exhibit a shear viscosity not very different to the solvent viscosity, i.e. $\eta_\infty = 1$mPa.s, the apparent Trouton ratio would be $Tr = O(100)$ and our observations are consistent with Batchelor (1971) who predicted that high aspect ratio particles can have extensional viscosities much larger than their shear viscosity. Interestingly, we observe high Trouton ratios even for our solutions containing soft, flexible, high aspect ratio GO sheets even though the analysis by Batchelor (1971) pertained to slender rod-like particles. For concentrations $\phi \geq 0.1$vol% we have dropped into a range of strain rates for which shear thinning is

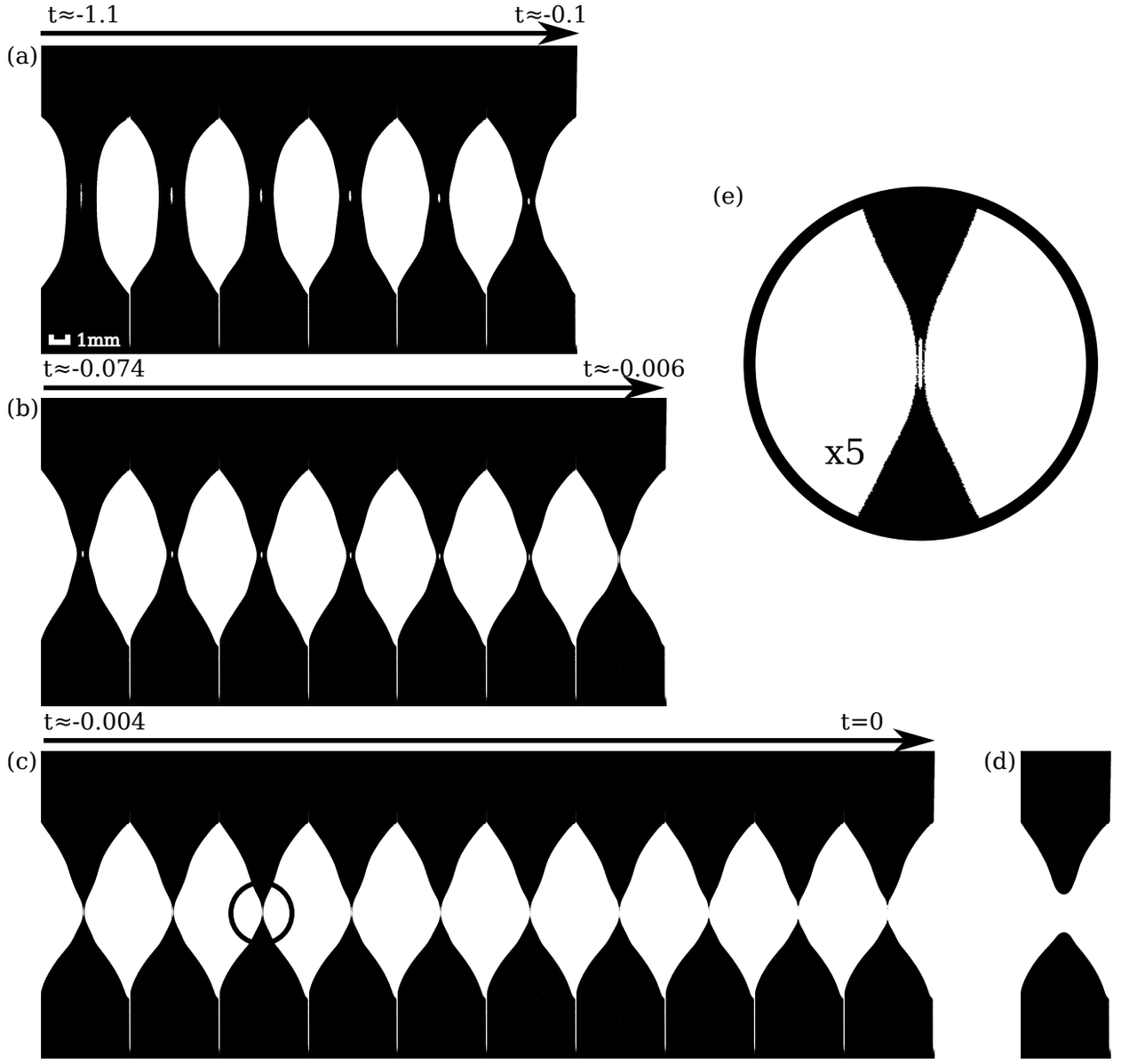

FIG. 6: An example image sequence for $\phi = 0.3$vol% and $h_f/h_0 = 3.78$ is shown, with $t = 0$ representing the time of filament breakup. (a) Then the piston stops and images show the initial stages of thinning with $\Delta t \approx 200$ms. (b) Intermediate stages of thinning with $\Delta t \approx 9.89$ms and (c) final thinning and breakup with $\Delta t \approx 0.35$s. (d) End-drops approximately $\Delta t = 2.83$ms after filament breakup. (e) Locally necked region in third image of bottom row at five time magnification.

observable, however, even at the highest concentration tested in the CaBER ($\phi = 0.3$vol%) the lowest strain rate encountered is $\dot{\epsilon} \approx 20\text{s}^{-1}$ which has a corresponding shear rate of $\dot{\gamma} \approx 35\text{s}^{-1}$. Here we can explain why the power-law exponents from CaBER measurements agree better with power-law exponents obtained from shear at earlier times in the filament evolution (figure 4d): the deformation rates only overlap at the earlier stages of filament thinning; at the latter stages of thinning the deformation rates encountered in extension

exceed those in shear measurements. For $\phi \geq 0.1$vol%, the apparent extensional viscosity does not monotonically increase with volume concentration for a given strain rate with $\eta_{app,ext}$ for $\phi = 0.2$vol% higher than that for $\phi = 0.3$vol% for all observable $\dot{\epsilon}$ even though the actual rate of filament thinning i.e. dR_{mid}/dt is significantly slower for $\phi = 0.3$vol%. Hence $\eta_{app,ext}$ being higher for $\phi = 0.2$vol% than $\phi = 0.3$vol% is likely due to the competing effects of viscosity and surface tension, which drops from $\sigma = 56 \pm 2\text{mNm}^{-1}$ at $\phi = 0.2$vol% to $\sigma = 29 \pm 2\text{mNm}^{-1}$ at $\phi = 0.3$vol%.
An important consequence of the continual shear rate thinning observed for $\phi \geq 0.1$vol% is that with a reducing viscosity, there exists the possibility of transitioning from a visco-capillary force balance to a visco-inertio-capillary balance. Hence, we consider a deformation-rate-dependent transient apparent Trouton ratio, i.e.;

$$Tr_{transient} = \frac{\eta_{app,ext}\left(\dot{\epsilon}\right)}{\eta\left(\dot{\gamma} = \sqrt{3}\dot{\epsilon}\right)}, \tag{10}$$

where we obtain the shear viscosity $\eta\left(\dot{\gamma} = \sqrt{3}\dot{\epsilon}\right)$ from steady shear measurements presented in section III. The transient apparent Trouton ratio is calculated for the range of deformation rates which are matched between the shear and CaBER experiments at each concentration and within the deformation rate range that is accessible $Tr_{transient}$ is nearly independent of the deformation rate with magnitudes of $Tr_{transient} \approx 30$, ≈ 18, ≈ 16 and ≈ 7 for concentrations of $\phi = 0.1$, 0.15, 0.2 and 0.3vol%, respectively (inset plot, figure 5). Interestingly, $Tr_{transient}$ is inversely related to the volume concentration suggesting that the GO flakes form increasingly strong networks in shear relative to extension with increasing volume concentration.

B. Laplace pressure profiles and an estimate of the apparent elongational yield stress

When calculating the Laplace pressure within the filaments we revert to using a step-stretch to form the filament and an image sequence depicting the capillary thinning and breakup of a GO filament with $\phi = 0.3$vol% is shown in figure 6. We see that immediately after the initial stretch (figure 6a), the thinning process is slow; in this example, it takes approximately $\Delta t \approx 1$s for the filament to display the conical tapering characteristic of yield-stress fluids. Between approximately $-0.1 \lesssim \Delta t \lesssim -0.006$s, the deformation process accelerates and we observe the onset of localized necking in the filament (figure 6b). Immediately leading up to ultimate breakup $\Delta t \gtrsim -4 \times 10^3$s (figure 6c), the necking point becomes very well defined and localized with the thinning process rapidly accelerating within this narrow region. The locally necked region, when shown at five times magnification (figure 6e), is seen to become transparent (except for light diffracted at the liquid/air interface) suggesting that there maybe migration of GO flakes away from the necked region towards the end-drops and that this concentration fluctuation leads to a localized reduction in viscosity (with an attendant change in surface tension) and hence accelerated thinning. A short time after filament breakup (figure 6d), the top of the end-drops take on a hemispherical shape. Valette et al. (2019) have referred to the conical meniscus prior to breakup as the signature of yield stress effects and the reemergence of hemi-spherical end-drops as the signature of capillary effects, respectively, and the presence of both in our observations is indicative of the competition between yield stress effects and capillarity in our test fluids. The corresponding time evolution of the filament minimum diameter is shown in figure 7 with the larger open circle symbols corresponding to the images displayed in figure 6. The filament diameter data has been smoothed for presentation purposes using a Savitzky-Golay filter, but even after smoothing, we can still see 'pixel-locking' in the early stages of thinning from oversampling temporally and an a slight error in locating the filament minimum diameter (which we do without recourse to curve fitting of the filament profiles along their axis). The filament thinning immediately after stretching is slow; appearing to thin linearly with time for $-1 \lesssim t \lesssim -0.4$s which is prior to the onset of the conical tapering

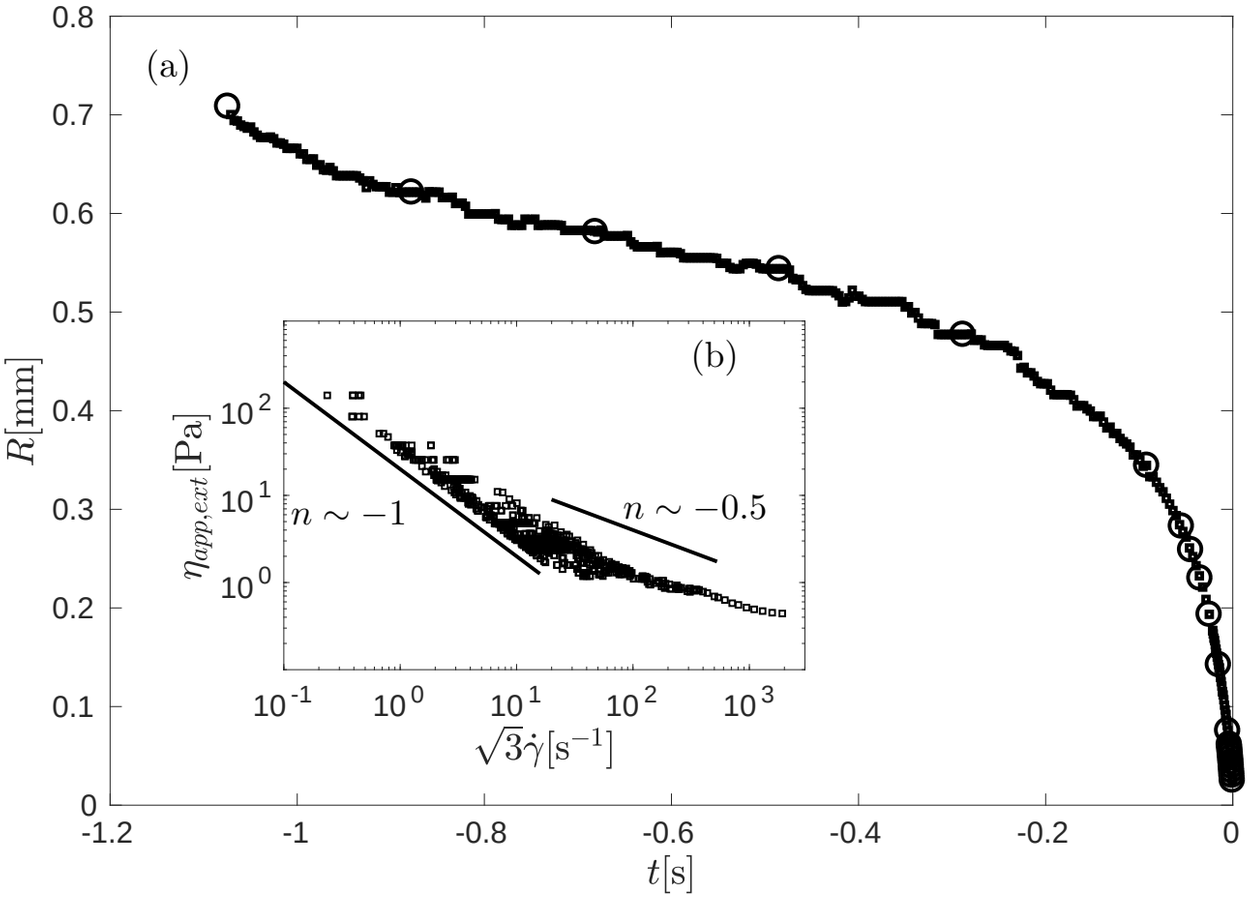

FIG. 7: (a) Time evolution of filament minimum diameter at height corresponding breakup for images shown in figures 6. Squares (□) are the full data set and circles (○) correspond to the actual images shown in figure 6. Here the filament minimum diameter is tracked in time without resorting to curve fitting and the filament diameter data presented here are smoothed using a Savitzky-Golay filter with a second-order polynomial and a fitting window of 13 points. (b) Estimate of $\eta_{app,ext}$ vs $\sqrt{3}\dot{\gamma}$ calculated from differentiation of filament time evolution in figure 7(a); although noisy, data appears to scale with exponent $n \sim -1$ at early stages of thinning transitioning to $n \sim -0.5$ at the later stages.

seen in the filament images. As the conical taper develops near, but not necessarily, at the filament mid-height, the thinning rate increases due to local necking (figure 6b); the thinning rate continues to increase and when very close to breakup ($\Delta t \gtrsim -4$ms), after the onset of a highly localized necked region, we see an acceleration in the filament thinning. From the time evolution of the diameter (figure 7a), we can calculate the apparent extensional viscosity $\eta_{app,ext}$ (figure 7b) which appears to scale roughly with an exponent of $n \sim -1$ in the early stages of thinning (low shear rates) and then transitions to an exponent of $n \sim -0.5$ at the later stages when the shear rates are more comparable to what was encountered using the SRM protocol. At the final stages of thinning (see figure 7b for $\sqrt{3}\dot{\epsilon} \gtrsim 10^3 \mathrm{s}^{-1}$); we observe that $\eta_{app,ext}$ begins to approach a constant value suggesting a return to Newtonian-like dynamics which corresponds to the onset of the locally necked region in figure 6(c). A scaling exponent of $n \sim -1$ at the early stages of thinning implies the aqueous GO solution with concentration $\phi = 0.3$vol% exhibits yield-stress-like behaviour in elongational flow. Although after yielding, it exhibits a power-law-like fluid response, the different response of aqueous GO samples when probed using a step stretch

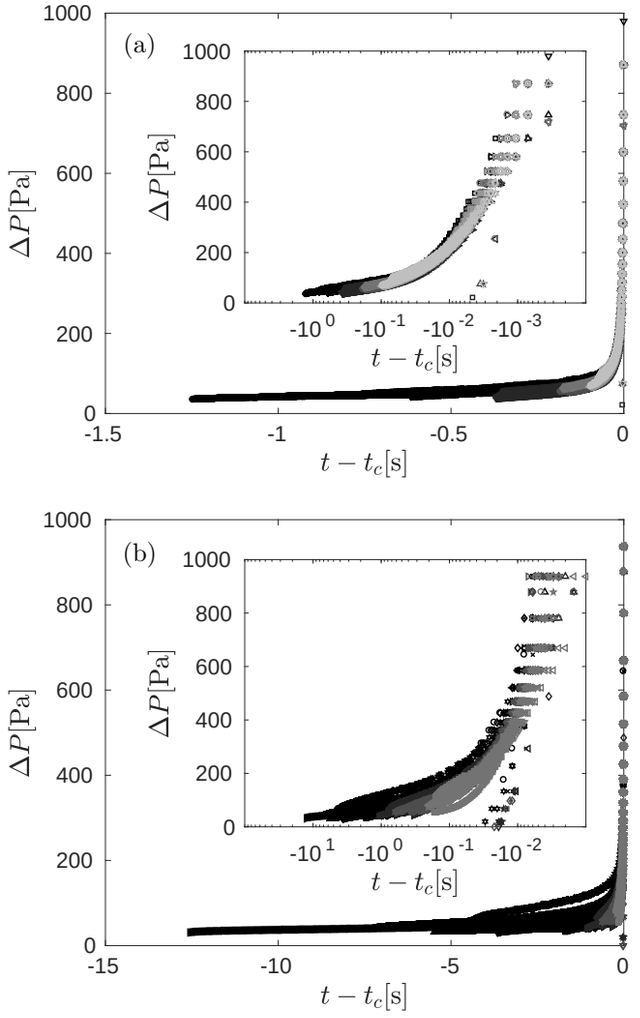

FIG. 8: Laplace pressure at location of filament minimum diameter ΔP plotted against time scaled with breakup time $t - t_c$. All measurements in campaign are plotted together here with each discrete shade of gray representing a given stretch ratio h_f/h_0. (a) $\phi = 0.3$vol% and (b) 0.4vol%. Insets show time on logarithmic axes.

and the measurements conducted with SRM protocol indicate that GO solutions are very sensitive to deformation history which reinforces what was observed in shear tests and this dependence on initial conditions is consistent with some other yield stress fluids. For example, Louvet et al. (2014) have reported that the thinning rate of Carbopol dispersions and castor-oil emulsions also depends on initial conditions but conclude that while those fluids behave differently for different initial conditions, they still behave as power-law fluids in the thinning dynamics.

The Laplace pressure profiles, calculated using equation (4), are plotted against time in figures 8(a) and 8(b) for volume concentrations $\phi = 0.3$ and 0.4vol%, respectively. All repeats for each stretch ratio are plotted together and the data have not been averaged due to the large variability in filament lifetime even for a fixed stretch ratio, which we believe are due to discrepancies in loaded sample volume. GO samples with volume concentration $\phi = 0.4$vol% were very difficult to load consistently into the CaBER using a pipette which contributed to the aforementioned variability in filament lifetime. The Laplace pressure is low initially, and then near breakup, it tends towards infinity as the filament radius R

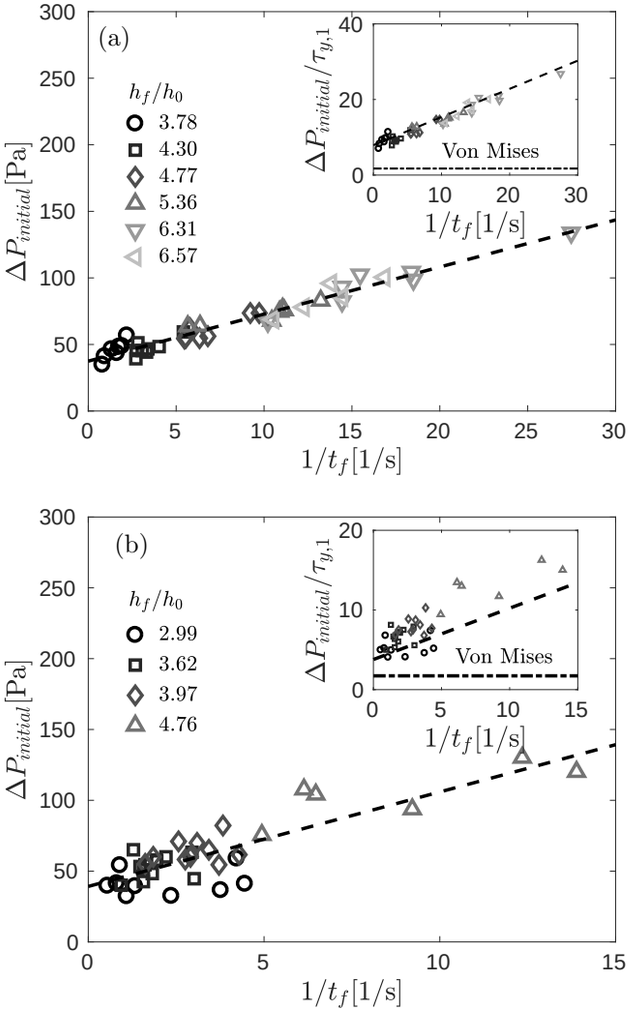

FIG. 9: Initial Laplace pressure $\Delta P_{initial}$ plotted against the inverse of filament lifetime $1/t_f$. Each symbol represents a measurements for a different stretch ratio h_f/h_0 and the spread indicates the error involved in controlling the volume loaded into the CaBER. Dashed lines represents linear fit to the data with an intercept of $\Delta P_{initial}|_{(t_f\to\infty)} = 37.4$Pa and 39.2Pa for $\phi = 0.30$vol% and 0.4vol%, respectively. The inset plots show the relative Laplace pressure $\Delta P_{initial}/\tau_{y,1}$ with the Von Mises plasticity criterion shown as the dot-dashed line.

becomes small whilst the filament curvature κ becomes large simultaneously. We see at long filament lifetimes, the initial Laplace pressure tends toward a constant value. The initial Laplace pressures (the average of the first ten values of each Laplace pressure profiles) scale linearly with the inverse of filament lifetime, $1/t_f$ (figure 9). Filament lifetimes tending towards infinity suggest an unyielded behaviour and we calculate an initial Laplace pressure as filament lifetime tends towards infinity by linear extrapolation. A linear trendline fitted to the data shown in figures 9(a,b) has an intercept of $\Delta P_{initial}|_{(t_f\to\infty)} = 37.4$Pa and 39.2Pa for volume concentrations of $\phi = 0.3$ and 0.4vol%, respectively, and we propose this as a simple proxy for the apparent elongational yield stress i.e. $\Delta P_{initial}|_{(t_f\to\infty)} \simeq \tau_{y,e}$ (in the absence of an extended plateau for the initial Laplace pressure shown in Martinie et al. (2013)). The inset plots show the *relative* initial Laplace pressure $\Delta P_{initial}/\tau_y$ where τ_y is the apparent shear yield stress determined from creep tests. The von Mises plasticity

criterion of $\tau_{y,e}/\tau_y = \sqrt{3}$ is drawn as a straight line in the inset plots. Martinie et al. (2013) strictly define that the elongational yield stress is the value of the initial Laplace pressure $\Delta P_{initial}$ at a Deborah number $De = t_R/t_f \approx 1$ where t_R is the longest shear relaxation time. In that study, t_R was determined from oscillatory shear measurements and identified as the inverse of the angular frequency ω for which the storage G' and loss G'' moduli were equivalent; i.e. $t_R = 1/\omega_{(G'=G'')}$. They demonstrate that *only* at $De \approx 1$ does the relative Laplace pressure agree well with the von Mises plasticity criterion for a range of yield stress materials. Due to the inherent thixotropy in our samples, and our need to pre-shear to obtain consistent shear results, we have not performed oscillatory shear flow measurements to determine our fluid relaxation times, therefore we cannot assess whether our simple proxy for apparent elongational yield stress of our GO solutions will obey the von Mises plasticity criterion at $De = 1$.

V. CONCLUSIONS

The shear and elongational rheology of aqueous graphene oxide solutions made of very large aspect ratio GO sheets, ($AR = O(10^4)$), dispersed in water with volume concentrations spanning $0.02 \leq \phi \leq 0.4$vol% was studied using shear-stress-controlled measurements with a parallel-plate geometry; and capillary breakup experiments in a commercial CaBER device. Creep experiments showed that a shear yield stress was measurable at concentrations $\phi \geq 0.10$vol% and shown to scale with concentration up to $\phi = 0.4$vol% according to a power-law relationship with exponent $n \sim 2.2$ in good agreement with exponents reported in the literature Vasu et al. (2013); Naficy et al. (2014); Del Giudice et al. (2018).
The extensional rheology of GO solutions was probed in a commercial CaBER device with filaments imaged using a high-speed camera. The acquired images reveals many interesting features of GO solutions subjected to uniaxial elongation. At the lowest concentration tested in CaBER $\phi = 0.02$vol% we observe a nearly purely inertia controlled breakup as we do for water with breakup appearing to occur at the end-drops. As concentrations increase to $\phi < 0.1$vol%; GO solutions exhibited Newtonian-like thinning dynamics with the filament diameter decreasing linearly with time (at the strain rates encountered). For $\phi \gtrsim 0.15$vol% the onset of conical tapering and localised necking were clearly visible, a signature of shear-thinning yield-stress-like behaviour. Power-law relationships fitted to the diameter evolution data yielded exponents in agreement with power-law exponents obtained in shear flow measurements at similar strain/shear rates. GO solutions which exhibit Newtonian breakup dynamics had apparent extensional viscosities in the range $100 \lesssim \eta_{app,ext} \lesssim 250$mPa.s. When strain rates in CaBER measurements overlapped the equivalent shear rates in shear experiments, the deformation-rate-dependent transient Trouton ratio appeared to be independent of strain rate, but inversely proportional to volume concentration, suggesting that for those same deformation rates; GO solutions form increasingly strong networks in shear with increasing concentration relative to the strength of the networks formed in uniaxial elongation. Following the methodology outlined by Martinie et al. (2013), we attempted to estimate the apparent elongational yield stress by calculating the initial Laplace pressure in the GO filaments formed in the CaBER using a step-stretch protocol with several different stretch ratios. The initial value of the Laplace pressure were found to decrease with increasing filament lifetimes t_f; and we extrapolated an initial Laplace pressure as filament lifetime tends to infinity of $\Delta P_{initial}|_{(t_f \to \infty)} \approx 37$ and 39Pa for GO solutions with volume concentration $\phi = 0.3$ and 0.4vol%, respectively. However, as it was not possible to reliably determine a relaxation time for our GO solutions, we are not able to calculate the Deborah number $De = t_R/t_f$ and hence cannot determine if our aqueous GO solutions comply with the von Mises plasticity criteria $\tau_{y,e}/\tau_y = \sqrt{3}$ at $De \approx 1$ which Martinie et al. (2013) reported to be the case for a range of other soft matter including highly concentrated emulsions, polymer gels and aggregated suspensions. In our step-stretch experiments, we observe that the rheological response given a fixed volume concentration differs to that from

experiments conducted using the slow retraction protocol Campo-Deaño and Clasen (2010) indicating that, while GO remains a power law fluid, it is highly sensitive to deformation history and initial conditions. We also observe that immediately prior to ultimate breakup, the fluid filament goes clear suggesting concentration fluctuations as GO flakes migrate away from the locally necked region. This appears to be well supported by the local acceleration in thinning rate very close to breakup.

Given that one cannot prescribe the strain rates in a CaBER experiment, as it is the fluid properties which select a self-similar force balance, our observation window is small due to the small timescales and very high strain rates encountered for GO solutions at these concentrations as a consequence of their low viscosities. A recently developed technique "Dripping-onto-Substrate" which can make accessible the capillary thinning and breakup dynamics of fluids with viscosities down to $\eta = 1$mPa.s it may be possible to extend this window. Even given the limitations discussed, we have in this work provided clear insight into the extensional rheology of aqueous GO solutions and demonstrate that the addition of even a very small amount of GO flakes can significantly alter the capillary thinning and pinch-off dynamics of a liquid bridge in comparison to Newtonian fluids of equivalent viscosity.

ACKNOWLEDGMENTS

R.J.P. would like to thank the EPSRC for the award of a Fellowship under grant number EP/M025187/1. We would also like to thank Prof. Eduardo Saiz (CASC, Department of Materials, Imperial College London) for facilitating the Graphene Oxide (GO) materials in this work; Prof. Phil Threlfall-Holmes (TH Collaborative Innovation) for useful discussions regarding the CaBER technique and Dr. David Dennis (University of Liverpool) for his assistance with image processing. The comments of the anonymous referees were extremely helpful in improving the paper and are hereby gratefully acknowledged.

REFERENCES

K. S. Novoselov, A. K. Geim, S. V. Morozov, D. Jiang, Y. Zhang, S. V. Dubonos, I. V. Grigorieva, and A. A. Firsov. Electric field effect in atomically thin carbon films. *Science*, 306(5696):666–669, 2004. ISSN 0036-8075. doi:10.1126/science.1102896.

A. K. Geim and K. S. Novoselov. The rise of graphene. *Nat. Mater.*, 6:183–191, 2007. doi:10.1038/nmat1849.

G. Eda, G. Fanchini, and M. Chhowalla. Large-area ultrathin films of reduced graphene oxide as a transparent and flexible electronic material. *Nat. Nanotechnol.*, 3:270–274, 2008. doi:10.1038/nnano.2008.83.

E. García-Tuñón, E. Feilden, H. Zheng, E. D'Elia, A. Leong, and E. Saiz. Graphene Oxide: An All-in-One Processing Additive for 3D Printing. *ACS Appl. Mater. Interfaces*, 9(38):32977–32989, 2017. doi:10.1021/acsami.7b07717.

M. K. Tiwari, A. V. Bazilevsky, A. L. Yarin, and C. M. Megaridis. Rheology and microstructure of dilute graphene oxide suspension. *J. Nanoparticle Res.*, 15:1989, 2013. doi:10.1007/s11051-013-1989-3.

K. S. Vasu, R. Krishnaswamy, S. Sampath, and A. K. Sood. Yield stress, thixotropy and shear banding in a dilute aqueous suspension of few layer graphene oxide platelets. *Soft Matter*, 9:5874–5882, 2013. doi:10.1039/c3sm50708d.

S. Naficy, R. Jalili, S. H. Aboutalebi, R. A. Gorkin III, K. Konstantinov, P. C. Innis, G. M. Spinks, P. Poulin, and G. G. Wallace. Graphene oxide dispersions: tuning rheology to enable fabrication. *Mater. Horiz.*, 1:326–331, 2014. doi:10.1039/c3mh00144j.

C. Vallès, R. J. Young, D. J. Lomaz, and I. A. Kinloch. The rheological behaviour of concentrated dispersions of graphene oxide. *J. Mater. Sci.*, 49:6311–6320, 2014. doi:10.1007/s10853-014-8356-3.

F. Del Giudice and A. Q. Shen. Shear rheology of graphene oxide dispersions. *Curr. Opin. Chem. Eng.*, 16:23 – 30, 2017.

F. Del Giudice, B. V. Cunning, R.S. Ruoff, and A. Q. Shen. Filling the gap between transient and steady shear rheology of aqueous graphene oxide dispersions. *Rheol. Acta*, 57:293–306, 2018. doi:10.1007/s00397-018-1077-9.

Z. Xu and C. Gao. Aqueous liquid crystals of graphene oxide. *ACS Nano*, 5(4):2908–2915, 2011. doi: 10.1021/nn200069w.

R. Jalili, S. H. Aboutalebi, D. Esrafilzadeh, R. L. Shepherd, J. Chen, S. Aminorroaya-Yamini, K. Konstantinov, A. I. Minett, J. M. Razal, and G. G. Wallace. Graphene Oxide: Scalable One-Step Wet-Spinning

of Graphene Fibers and Yarns from Liquid Crystalline Dispersions of Graphene Oxide: Towards Multifunctional Textiles. *Adv. Funct. Mater.*, 23(43):5344–5344, 2013. doi:10.1002/adfm.201370222.

P. Kumar, U. N. Maiti, K. E. Lee, and S. O. Kim. Rheological properties of graphene oxide liquid crystal. *Carbon*, 80:453–461, 2014. doi:10.1016/j.carbon.2014.08.085.

C. Cheng and D. Li. Solvated Graphenes: An Emerging Class of Functional Soft Materials. *Adv. Mater.*, 25(1):13–30, 2013. doi:10.1002/adma.201203567.

M. J. Allen, V. C. Tung, and R. B. Kaner. Honeycomb carbon: A review of graphene. *Chem. Rev.*, 110(1): 132–145, 2010. doi:10.1021/cr900070d.

P Poulin, R. Jalili, W. Neri, F. Nallet, T. Divoux, A. Colin, S. H. Aboutalebi, G. Wallace, and C. Zakri. Superflexibility of graphene oxide. *Proc. Natl. Acad. Sci. U.S.A.*, 113(40):11088–11093, 2016. ISSN 0027-8424. doi:10.1073/pnas.1605121113. URL `https://www.pnas.org/content/113/40/11088`.

C. Chen, Q.-H. Yang, Y. Yang, L. Wei, Y. Wen, P.-X. Hou, M. Wang, and H.-M. Cheng. Self-assembled free-standing graphite oxide membrane. *Adv. Mater.*, 21(29):3007–3011, 2009. doi:10.1002/adma.200803726.

J. Kim, L. J. Cote, F. Kim, W. Yuan, K. R. Shull, and J. Huang. Graphene oxide sheets at interfaces. *J. Am. Chem. Soc.*, 132(23):8180–8186, 2010a. doi:10.1021/ja102777p.

F. Kim, L. J. Cote, and J. Huang. Graphene oxide: Surface activity and two-dimensional assembly. *Adv. Mater.*, 22(17):1954–1958, 2010b. doi:10.1002/adma.200903932. URL `https://onlinelibrary.wiley.com/doi/abs/10.1002/adma.200903932`.

J. P. Hartnett and R. Y. Z. Hu. Technical note: The yield stress— An engineering reality. *J. Rheol.*, 33(4): 671–679, 1989. doi:10.1122/1.550006.

Q. D. Nguyen and D. V. Boger. Measuring the flow properties of yield stress fluids. *Annu. Rev. Fluid. Mech.*, 24(1):47–88, 1992. doi:10.1146/annurev.fl.24.010192.000403.

D. Bonn and M. M. Denn. Yield Stress Fluids Slowly Yield to Analysis. *Science*, 324(5933):1401–1402, 2009. doi:10.1126/science.1174217.

N. J. Balmforth, I. A. Frigaard, and G. Ovarlez. Yielding to Stress: Recent Developments in Viscoplastic Fluid Mechanics. *Annu. Rev. Fluid. Mech.*, 46(1):121–146, 2014. doi:10.1146/annurev-fluid-010313-141424.

K. Niedzwiedz, O. Arnolds, N. Willenbacher, and R. Brummer. How to Characterize Yield Stress Fluids with Capillary Breakup Extensional Rheometry (CaBER)? *Appl. Rheol.*, 19:41969, 2009.

K. Niedzwiedz, H. Buggisch, and N. Willenbacher. Extensional rheology of concentrated emulsions as probed by capillary breakup elongational rheometry (CaBER). *Rheol. Acta*, 49:1103–1116, 2010. doi: 10.1007/s00397-010-0477-2.

N. J. Balmforth, N. Dubash, and A. C. Slim. Extensional dynamics of viscoplastic filaments: II. Drips and bridges. *J. Nonnewton. Fluid Mech.*, 165:1147– 1160, 2010. doi: https://doi.org/10.1016/j.jnnfm.2010.06.004.

L. Martinie, H. Buggisch, and N. Willenbacher. Apparent elongational yield stress of soft matter. *J. Rheol.*, 57(2):627–646, 2013. doi:10.1122/1.4789785.

N. Louvet, D. Bonn, and H. Kellay. Nonuniversality of the Pinch-Off of Yield Stress Fluids: Role of Nonlocal Rheology. *Phys. Rev. Lett.*, 113:218302, Nov 2014. doi:10.1103/PhysRevLett.113.218302.

R. Valette, E. Hachem, M. Khalloufi, A.S. Pereira, M.R. Mackley, and S.A. Butler. The effect of viscosity, yield stress, and surface tension on the deformation and breakup profiles of fluid filaments stretched at very high velocities. *J. Nonnewton. Fluid Mech.*, 263:130–139, 2019. ISSN 0377-0257. doi:https://doi.org/10.1016/j.jnnfm.2018.12.001.

B. J. Lowry and P. H. Steen. Capillary surfaces: stability from families of equilibria with application to the liquid bridge. *Proc. Royal Soc. A*, 449(1937):411–439, 1995. doi:10.1098/rspa.1995.0051.

M. P. Mahajan, M. Tsige, P. L. Taylor, and C. Rosenblatt. Stability of liquid crystalline bridges. *Phys. Fluids*, 11(2):491–493, 1999. doi:10.1063/1.869871.

A. Corker, H. C.-H. Ng, R. J. Poole, and E. García-Tuñón. 3D printing with 2D colloids: designing rheology protocols to predict 'printability' of soft-materials. *Soft Matter*, 2019. doi:10.1039/C8SM01936C.

E. García-Tuñón, S. Barg, J. Franco, R. Bell, S. Eslava, E. DÉlia, R. C. Maher, F. Guitian, and E. Saiz. Printing in Three Dimensions with Graphene. *Adv. Mater.*, 27(10):1688–1693, 2015. doi: 10.1002/adma.201405046.

V. G. Rocha, E. García-Tuñón, C. Botas, F. Markoulidis, E. Feilden, E. DÉlia, N. Ni, M. Shaffer, and E. Saiz. Multimaterial 3D Printing of Graphene-Based Electrodes for Electrochemical Energy Storage Using Thermoresponsive Inks. *ACS Appl. Mater. Interfaces*, 9(42):37136–37145, 2017. doi:10.1021/acsami.7b10285.

G. H. McKinley and A. Tripathi. How to extract the Newtonian viscosity from capillary breakup measurements in a filament rheometer. *J. Rheol.*, 44(3):653–670, 2000. doi:10.1122/1.551105.

S. L. Anna and G. H. McKinley. Elasto capillary thinning and breakup of model elastic liquids. *J. Rheol.*, 45(2):115–138, 2001.

D. T. Papageorgiou. On the breakup of viscous liquid threads. *Phys. Fluids*, 7(7):1529–1544, 1995. doi: 10.1063/1.868540.

V. M. Entov and E. J. Hinch. Effect of a spectrum of relaxation times on the capillary thinning of a filament of elastic liquid. *J. Nonnewton. Fluid Mech.*, 97:31 – 53, 1997.

L. Campo-Deaño and C. Clasen. The slow retraction method (SRM) for the determination of ultra-short relaxation times in capillary breakup extensional rheometry experiments. *J. Nonnewton. Fluid Mech.*, 165(23):1688 – 1699, 2010. doi:https://doi.org/10.1016/j.jnnfm.2010.09.007.

J. Canny. A computational approach to edge detection. *IEEE Trans. Pattern Anal. Mach. Intell.*, PAMI-8 (6):679–698, 1986.

M. Dinkgreve, J. Paredes, M. M. Denn, and D. Bonn. On different ways of measuring "the" yield stress. *J. Nonnewton. Fluid Mech.*, 238:233 – 241, 2016. ISSN 0377-0257.

R. F. Day, E. J. Hinch, and J. R. Lister. Self-similar capillary pinchoff of an inviscid fluid. *Phys. Rev. Lett.*, 80:704–707, 1998.

J Eggers. Universal pinching of 3D axisymmetric free-surface flow. *Phys. Rev. Lett.*, 71:3458–3460, 1993.

L. E. Rodd, T. P. Scott, J. J. Cooper-White, and G. H. McKinley. Capillary break-up rheometry of low-viscosity elastic fluids. *Appl. Rheol.*, 15:12–27, 2005.

J. Dinic, L. N. Jimenez, and V. Sharma. Pinch-off dynamics and dripping-onto-substrate (DoS) rheometry of complex fluids. *Lab Chip*, 17:460–473, 2017.

S. Sur and J. Rothstein. Drop breakup dynamics of dilute polymer solutions: Effect of molecular weight, concentration, and viscosity. *J. Rheol.*, 62(5):1245–1259, 2018. doi:10.1122/1.5038000.

G. H. McKinley. Visco-elasto-capillary thinning and breakup of complex fluid. *British Soc. Rheol.*, pages 1–49, 01 2005.

G. K. Batchelor. The stress generated in a non-dilute suspension of elongated particles by pure straining motion. *J. Fluid Mech.*, 46(4):813–829, 1971. doi:10.1017/S0022112071000879.

πάντα ῥεῖ

Journal of Rheology

ACCEPTED MANUSCRIPT

PLEASE CITE THIS ARTICLE AS DOI: 10.1122/1.5109016

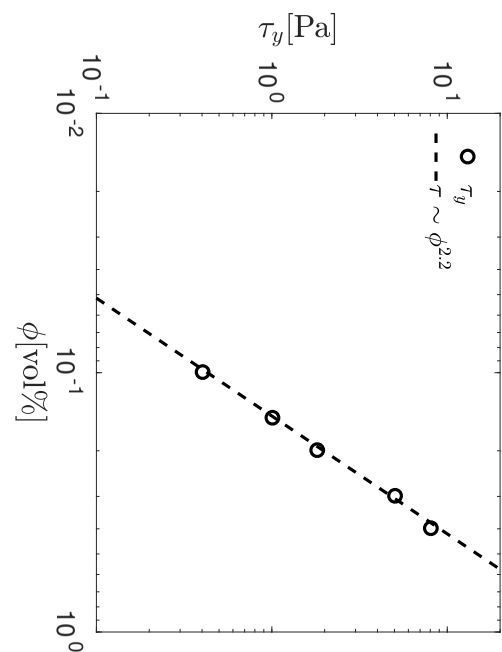

Journal of Rheology ACCEPTED MANUSCRIPT

PLEASE CITE THIS ARTICLE AS DOI: 10.1122/1.5109016

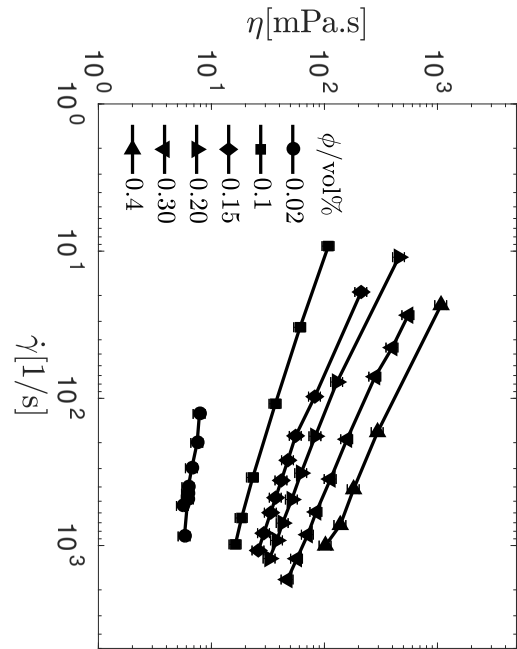

Journal of Rheology

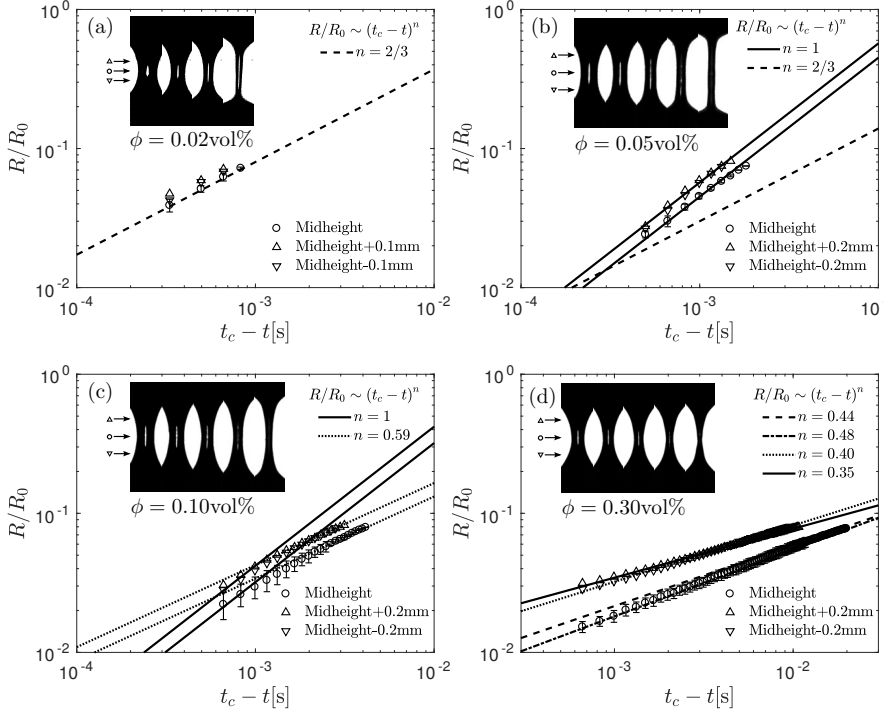

πάντα ῥεῖ

Journal of Rheology

ACCEPTED MANUSCRIPT

PLEASE CITE THIS ARTICLE AS DOI: 10.1122/1.5109016

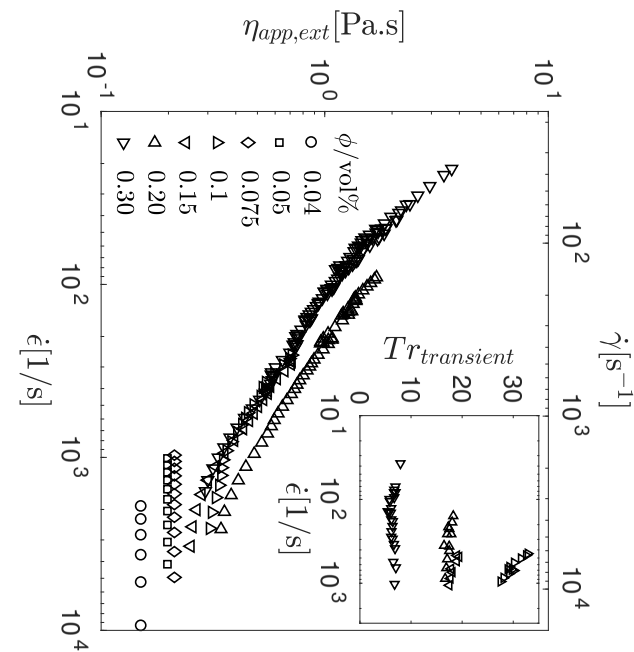

Journal of Rheology

PLEASE CITE THIS ARTICLE AS DOI: 10.1122/1.5109016

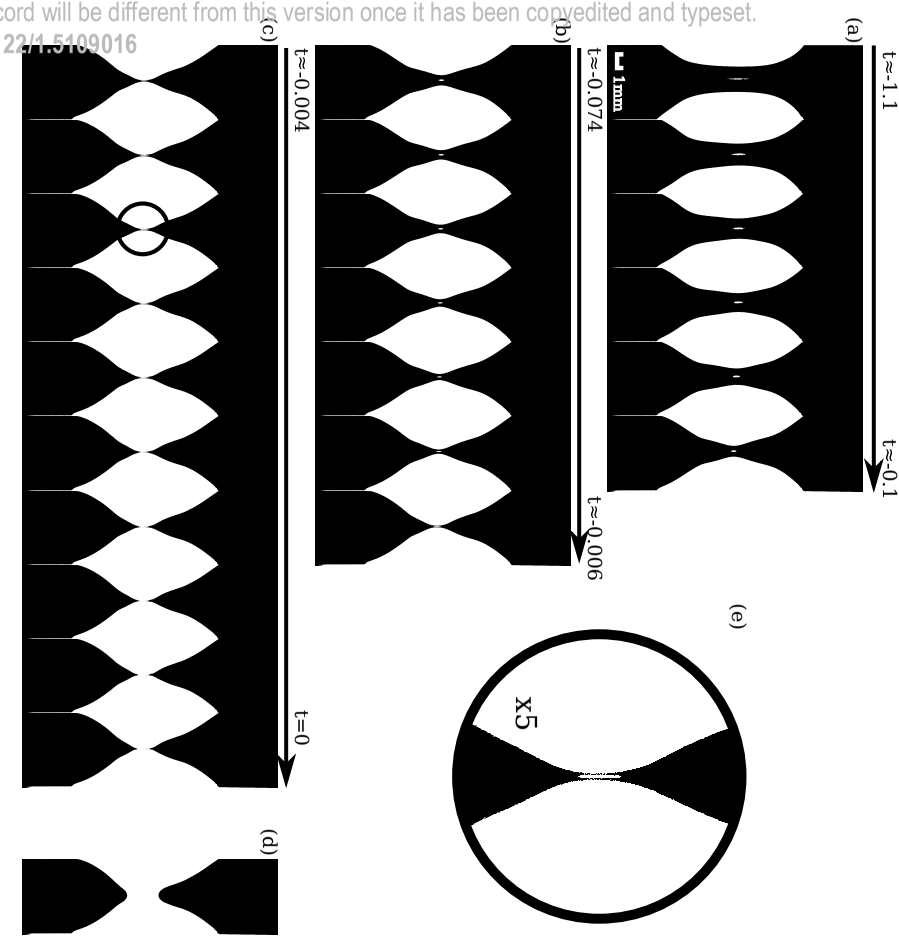

πάντα ῥεῖ

Journal of Rheology

ACCEPTED MANUSCRIPT

PLEASE CITE THIS ARTICLE AS DOI: 10.1122/1.5109016

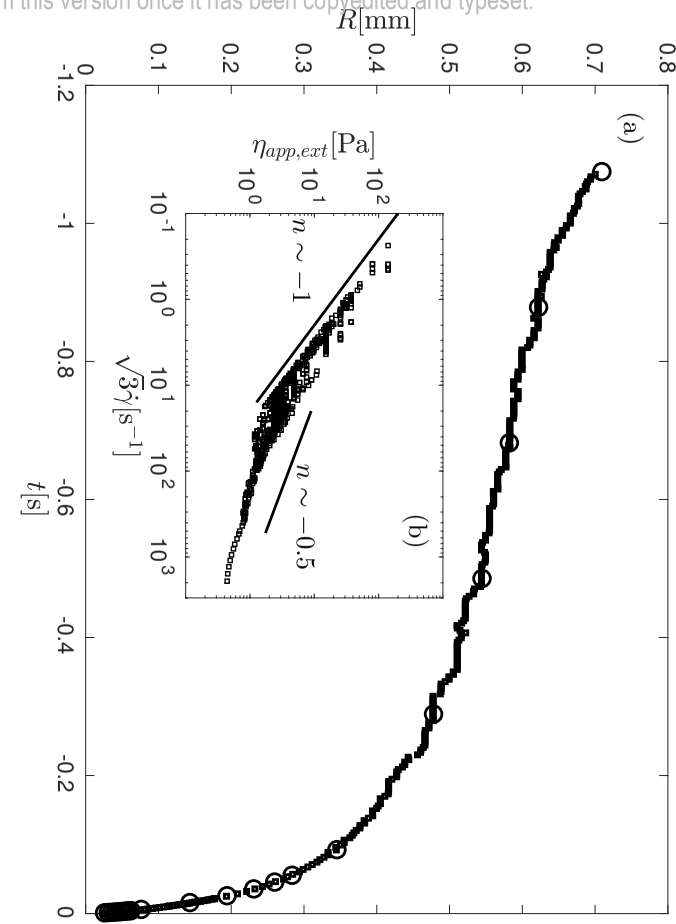

Journal of Rheology ACCEPTED MANUSCRIPT

PLEASE CITE THIS ARTICLE AS DOI: 10.1122/1.5109016